MODELING AND SIMULATION OF STRATIFIED CURRENTS WITH ROTATION EFFECTS

Jorge S. Salinas[a]**, Mariano I. Cantero**[a,b,c] **and Daniela Arnica**[c]

[a]*Institute Balseiro, San Carlos de Bariloche, Río Negro, Argentina.*

[b]*National Council for Scientific and Technological Research, San Carlos de Bariloche, Río Negro, Argentina.*

[c]*Bariloche Atomic Center, National Commission of Atomic Energy, San Carlos de Bariloche, Río Negro, Argentina.*

Keywords: Density Currents, Rotation Effects, Turbulent Flows, Direct Numerical Simulation.

Abstract. Stratified currents are generated by action of gravity (or other volumetric force) on changes in fluid density. When they appear in turbulent regime, stratified currents are of a non-linear nature and have a wide range of temporal and spatial scales. In these systems there is a strong coupling between turbulence and stratification effects, with important consequences in the exchange of mass, momentum and energy. When these type of flows happen in geophysical scale, the analysis is further complicated by the influence of rotation effects, as is the case for example of volcanic plumes influenced by Coriolis forces originated by earth's rotation. In this work we study stratified currents in a channel with rotation effects by direct numerical simulations. We compare different conditions of rotation, and report on the maximum length of the leading edge of the successive outward propagating fronts, the pulse frequency, and the different phases of spreading.

1   INTRODUCTION

Stratified currents manifest as a horizontal current of heavy fluid running below light fluid, or as a current of light fluid running above heavy fluid. These currents are buoyancy-driven flows and can be produced with very small density differences, yet they may become powerful and strong flows (García, 1992). These types of flows are also known as density or gravity currents.

On a large scale, stratified currents play an important role in the circulation of the atmosphere and hydrosphere over a large range of scales and geometric configurations (Droegemeier and Wilhelmson, 1986, 1987). Stratified currents are also the mean by which oil spills are spread in the ocean (Fay, 1969; Fannelop and Waldman, 1971; Hoult, 1972). In all these examples the effect of earth rotation is important and manifests mainly by the Coriolis force affecting the flows Ungarish (2009). On a smaller scale, the deliberate (and generally more rapid) rotation of fluids in certain industrial processes can have either advantageous or detrimental consequences for the desired process.

A large amount of research has been conducted to address the spreading characteristics of stratified currents (see Benjamin, 1968; Fannelop and Waldman, 1971; Hoult, 1972; Huppert and Simpson, 1980; Choi and García, 2002; Cantero et al., 2007b, for example). Huppert and Simpson (1980) described the spreading of gravity currents in three phases: an initial slumping phase where the current moves at nearly constant speed, followed by an inertial phase in which the current moves under the balance of buoyancy and inertial forces, and a final viscous phase where viscous effects dominate and balance buoyancy. Cantero et al. (2007b) revisited the different scaling laws for the all the phases of spreading and, by means of direct numerical simulations and experimental data, explained in detail the transition between them.

This work addresses the characteristics of currents spreading under the influence of rotation effects by direct numerical simulation. More precisely, the work focuses on the behavior of planar stratified currents, produced in a rectangular horizontal rotating channel, and describes the time evolution of front location and velocity for the different phases of spreading.

2   MATHEMATICAL AND NUMERICAL FORMULATION

2.1   Mathematical formulation

The system under consideration is depicted schematically in Fig. 1. The system consists of a periodic channel that rotates with constant angular velocity Ω_z along the vertical axis (z). The channel is of height H and the periodic boundaries are placed at $y = 0$ and $y = D$. At the start of the computation the region with heavy fluid of density ρ_1 (the gray shaded region in Fig. 1) is separated from the light ambient co-rotating fluid of density ρ_0. The heavy fluid is a slab of half-width x_0 along the flow direction (x). In the present simulations, the slab of heavy fluid extends over the entire height H of the channel (full-depth release) and along the spanwise (y) direction.

We consider flows in which the density difference is small enough that the Boussinesq approximation is valid. Under these circumstances and in a system of reference attached to the channel, the flow is governed by the following equations

$$\frac{\partial \mathbf{u}}{\partial t} + \mathbf{u} \cdot \nabla \mathbf{u} = -\frac{1}{\rho_0}\nabla p + \nu \nabla^2 \mathbf{u} + \frac{\rho - \rho_0}{\rho_0}\,\mathbf{g} - 2\mathbf{\Omega} \times \mathbf{u} - \mathbf{\Omega} \times (\mathbf{\Omega} \times \mathbf{r})\,, \qquad (1)$$

$$\nabla \cdot \mathbf{u} = 0\,, \qquad (2)$$

$$\frac{\partial \rho}{\partial t} + \mathbf{u} \cdot \nabla \rho = \kappa\,\nabla^2 \rho\,, \qquad (3)$$
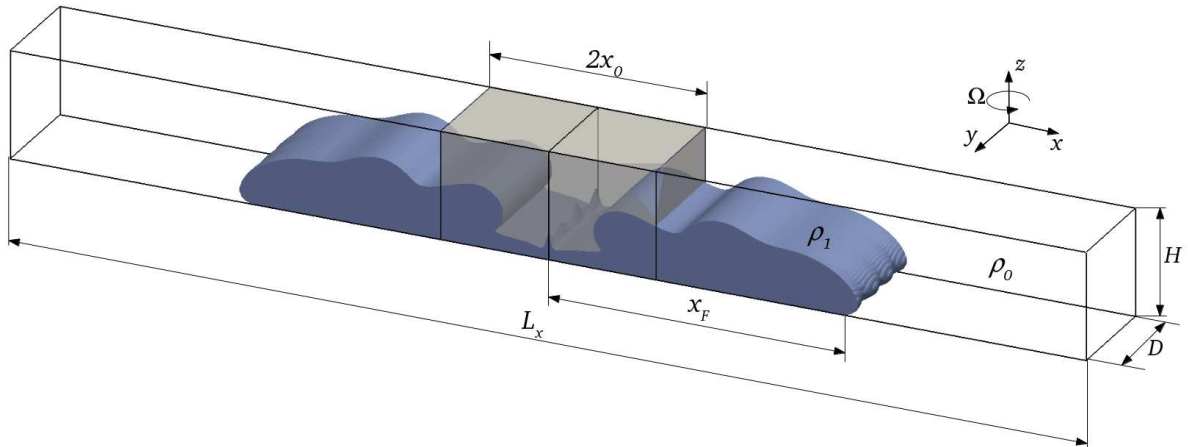
Figure 1: Schematic of the configuration for the planar system.

where $\mathbf{u} = \{u, v, w\}$ is the velocity vector, $\mathbf{r} = x\hat{\mathbf{x}} + y\hat{\mathbf{y}} + z\hat{\mathbf{z}}$ is the position vector, p is the pressure, ν is the kinematic viscosity, $\mathbf{g} = \{0, 0, -g_z\}$ is the acceleration due to gravity, ρ the density of the mixture, κ the diffusivity, and $\mathbf{\Omega} = \{0, 0, \Omega_z\}$ the constant angular velocity.

2.2 Dimensionless equations

For the dimensionless form of the equations (1)-(3), we employ the length scale H, the velocity scale $U = \sqrt{RgH}$ with $R = (\rho_1 - \rho_0)/\rho_0$, and the time scale $T = H/U$. The dimensionless density is given by

$$\tilde{\rho} = \frac{\rho - \rho_0}{\rho_1 - \rho_0}. \tag{4}$$

Then, for (1) - (3) we have

$$\frac{\partial \tilde{\mathbf{u}}}{\partial \tilde{t}} + \tilde{\mathbf{u}} \cdot \tilde{\nabla}\tilde{\mathbf{u}} = -\tilde{\nabla}\tilde{p} + \frac{1}{Re}\tilde{\nabla}^2\tilde{\mathbf{u}} - \tilde{\rho}\,\hat{\mathbf{z}} - (1 + R\tilde{\rho})2\tilde{\mathcal{C}}(\tilde{v}\hat{\mathbf{x}} - \tilde{u}\hat{\mathbf{y}}) - R\tilde{\mathcal{C}}^2\tilde{\rho}(\tilde{x}\hat{\mathbf{x}} + \tilde{y}\hat{\mathbf{y}}), \tag{5}$$

$$\tilde{\nabla} \cdot \tilde{\mathbf{u}} = 0, \tag{6}$$

$$\frac{\partial \tilde{\rho}}{\partial \tilde{t}} + \tilde{\mathbf{u}} \cdot \tilde{\nabla}\tilde{\rho} = \frac{1}{Re\,Sc}\tilde{\nabla}^2\tilde{\rho}. \tag{7}$$

Here, $\tilde{\mathbf{u}} = \{\tilde{u}, \tilde{v}, \tilde{w}\}$ is the dimensionless velocity, $\tilde{p}$ the dimensionless pressure, and the dimensionless parameters are the Reynolds, Schmidt, and Coriolis numbers defined as

$$Re = \frac{U H}{\nu}, \qquad Sc = \frac{\nu}{\kappa} \quad \text{and} \quad \tilde{\mathcal{C}} = \frac{\Omega H}{U}. \tag{8}$$

Because we consider flows in which the density difference is small enough that the Boussinesq approximation is valid ($\rho \approx \rho_0$ for inertial forces), it follows that $R\tilde{\mathcal{C}}^2 \ll 1$ and $(1+R\tilde{\rho}) \approx 1$. With these approximations the centrifugal term in (5) is negligible, and (5) - (7) yield

$$\frac{\partial \tilde{\mathbf{u}}}{\partial \tilde{t}} + \tilde{\mathbf{u}} \cdot \tilde{\nabla}\tilde{\mathbf{u}} = -\tilde{\nabla}\tilde{p} + \frac{1}{Re}\tilde{\nabla}^2\tilde{\mathbf{u}} - \tilde{\rho}\,\hat{\mathbf{z}} - 2\tilde{\mathcal{C}}(\tilde{v}\hat{\mathbf{x}} - \tilde{u}\hat{\mathbf{y}}), \tag{9}$$

$$\tilde{\nabla} \cdot \tilde{\mathbf{u}} = 0, \tag{10}$$

$$\frac{\partial \tilde{\rho}}{\partial \tilde{t}} + \tilde{\mathbf{u}} \cdot \tilde{\nabla}\tilde{\rho} = \frac{1}{Re\,Sc}\tilde{\nabla}^2\tilde{\rho}. \tag{11}$$

The ratio x_0/H is an additional geometric parameter that controls the volume of initial release. In our simulations, we consider the case of $H = x_0$.

2.3   Numerical formulation

The governing equations are solved in a dimensionless rectangular box of size $\tilde{L}_x \times \tilde{D} \times \tilde{H}$. Periodic boundary conditions are employed along the streamwise ($\tilde{x}$) and spanwise ($\tilde{y}$) directions. The periodic channel is taken to be long enough along the streamwise direction in order to allow free unhindered development of the current for a long time.

In this work, we have employed a fully de-aliased pseudo-spectral code (Canuto et al., 1988), in which Fourier expansions are employed for the flow variables along the horizontal directions ($\tilde{x}$ and $\tilde{y}$). In the inhomogeneous vertical direction ($\tilde{z}$), a Chebyshev expansion is used with Gauss-Lobatto quadrature points (Canuto et al., 1988). The flow field is time advanced using a Crank-Nicolson scheme for the diffusion terms. The advection terms are handled with the Arakawa method (Durran, 1999) and advanced with a third-order Runge-Kutta scheme. The buoyancy term is also advanced with a third-order Runge-Kutta scheme. At the top and bottom walls, no-slip and zero-gradient conditions are enforced for velocity and concentration, respectively. Detailed implementation can be found in (Cantero et al., 2006, 2007b,a).

3   THEORETICAL BACKGROUND

In this section, we present a brief description of the models that predict the front velocity during the slumping, inertial and viscous phases for the case of non-rotating flows.

3.1   Slumping phase

In the slumping phase, the front of the current moves at nearly constant speed. The hydraulic theories for non-rotating currents give $\tilde{u}_F = 0.5$ (Benjamin, 1968; Shin et al., 2004) where $\tilde{u}_F$ is the front velocity. Based on laboratory experiments, Huppert and Simpson (1980) report $\tilde{u}_F \approx 0.45$, and Cantero et al. (2007b), based on DNS simulations and experimental data, report $\tilde{u}_F = 0.45$. Cantero et al. (2007b) argued that the departure from hydraulic theories owes to the expenditure of energy to set up internal motion of the current.

3.2   Inertial phase

Transition from the slumping to the inertial phase occurs when the reflected back- propagating wave catches up with the front (Rottman and Simpson, 1983). It is accepted that for a planar current in non-rotating systems the transition happens after the front has traveled between 5 and 9 lock lengths (Rottman and Simpson, 1983; Metha et al., 2002; Marino et al., 2005). The asymptotic behavior of the current in the inertial phase has been established to be (Fay, 1969; Fannelop and Waldman, 1971; Hoult, 1972; Huppert and Simpson, 1980; Rottman and Simpson, 1983)

$$\tilde{x}_F = \xi_p(\tilde{h}_0\tilde{x}_0\tilde{t}^2)^{1/3}\,, \qquad \tilde{u}_F = \frac{2}{3}\xi_p(\tilde{h}_0\tilde{x}_0)^{1/3}\tilde{t}^{-1/3}\,. \tag{12}$$

Here, $\tilde{x}_F$, $\tilde{x}_0$ and $\tilde{h}_0$ are the dimensionless streamwise location of the front of the current, the initial height of the release, and the initial length of release, respectively. The difference between the theories is in the constant ξ_p. In our study, we use the value $\xi_p = 1.47$ proposed by Cantero et al. (2007b).

3.3 Viscous phase

By balancing the buoyancy and viscous forces over the interface between the heavy and light fluids and a rigid horizontal surface, Huppert (1982) obtained the resulting self-similar solutions for the viscous phase

$$\tilde{x}_F = \xi_{pHp}\tilde{h}_0^{3/5}\tilde{x}_0^{3/5}Re^{1/5}\tilde{t}^{1/5}\,, \qquad \tilde{u}_F = \frac{1}{5}\xi_{pHp}\tilde{h}_0^{3/5}\tilde{x}_0^{3/5}Re^{1/5}\tilde{t}^{-4/5}\,. \tag{13}$$

In our study, we use the value $\xi_{pHp} = 3.2$ proposed by Cantero et al. (2007b).

4 RESULTS AND DISCUSSION

The dimensions of the domains in all simulations with rotation ($\tilde{\mathcal{C}} \neq 0$) presented in this work are $\tilde{L}_x \times \tilde{D} \times \tilde{H} = 18 \times 1 \times 1$, with a resolution $N_x \times N_y \times N_z = 768 \times 64 \times 128$. For the simulation without rotation ($\tilde{\mathcal{C}} = 0$), we use $\tilde{L}_x \times \tilde{D} \times \tilde{H} = 25 \times 1 \times 1$, with a resolution $N_x \times N_y \times N_z = 924 \times 56 \times 110$. The rest of the parameters are shown in Table. 1 .

case	$\tilde{\mathcal{C}}$	Re	Sc	$\tilde{x}_0$	$\overline{x}_{max}$	$\overline{\omega}_p$
0	0	2000	1	1	-	-
1	0.1	2000	1	1	7.5	0.20
2	0.15	2000	1	1	5.25	0.31
3	0.25	2000	1	1	3.38	0.50

Table 1: Numerical simulations performed for this paper. Also shown are the values of the maximum distance attained by the first propagating front ($\overline{x}_{max}$) and the frequency of the subsequent fronts for the rotating currents, $\overline{\omega}_p$.

4.1 Current height

The height of the current can be defined in a few different ways. Shin et al. (2004) and Marino et al. (2005) define a local equivalent height in an unambiguous way as

$$\tilde{h}(\tilde{x}, \tilde{y}, \tilde{t}) = \int_0^1 \tilde{\rho}\,d\tilde{z}\,, \tag{14}$$

and this definition is adopted herein. Thus, at locations where the entire layer is occupied by the heavy fluid, the dimensionless height is unity, whereas at locations where the light fluid fills the entire layer, the height is zero. The local current height can then be averaged over the spanwise direction. We define the span-averaged current height as

$$\overline{h}(\tilde{x}, \tilde{t}) = \frac{1}{\tilde{L}_y}\int_0^{\tilde{L}_y} \tilde{h}\,d\tilde{y}\,. \tag{15}$$

(Any variable with an overbar is to be understood as dimensionless span-averaged quantity).

4.2 Mean front location and velocity

The mean front location, $\overline{x}_F$, can be unambiguously defined as the location where the span-averaged equivalent height, $\overline{h}$, becomes smaller than a small threshold δ. Precise definition can be found in Cantero et al. (2007b). The mean front velocity is computed as

$$\overline{u}_F = \frac{d\overline{x}_F}{d\tilde{t}}\,. \tag{16}$$

The front velocity $\overline{u}_F$ as a function of time $\tilde{t}$ for all cases with different Coriolis parameter $\tilde{\mathcal{C}}$ are shown in figures 2 and 3 together with the different scaling laws. We can observe a clear influence of rotation in all the phases of spreading.
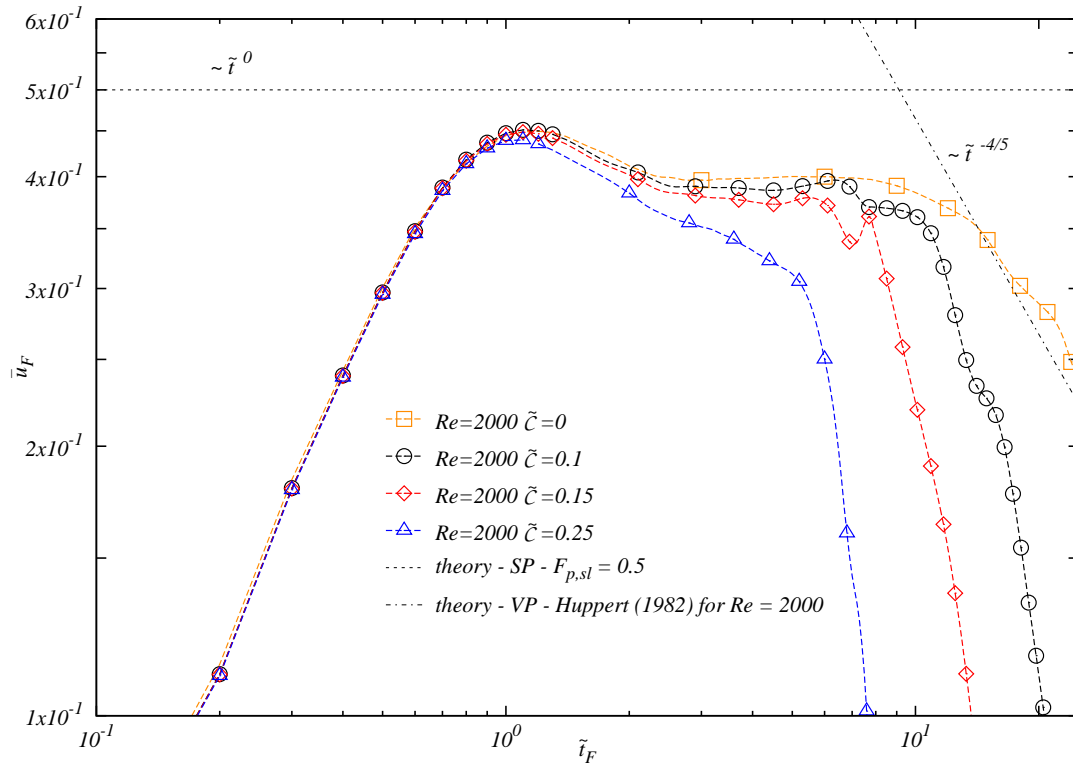

Figure 2: Front velocity $\overline{u}$ as a function of time $\tilde{t}$. Figure also include the scaling laws for the slumping and viscous phases.

4.2.1 Acceleration phase

After the heavy fluid is released, the front velocity increases until a maximum, and then drops to the slumping phase constant velocity, as shown in Fig. 2. This initial phase is called the acceleration phase. The location where the peak velocity happens is insensitive to $\tilde{\mathcal{C}}$. The same happens for the time at which the peak velocity is reached. The maximum velocity occurs at about $\overline{x}_F - \overline{x}_0 = 0.3$ and at $\tilde{t} = 1.1$ for all cases.

The value of the peak, however, is influenced and a significant drop is observed with increasing $\tilde{\mathcal{C}}$. The peak values are 0.451, 0.449 and 0.439 for $\tilde{\mathcal{C}} = 0.1$, 0.15 and 0.25, respectively.

In our simulations we study the idealized initial condition of instantaneous release of the dense fluid. During the acceleration phase, three-dimensional disturbances has not grown to sufficient amplitude, and because of this, the current is mostly two-dimensional.

4.2.2 Slumping phase

As we mentioned in the previous section, after the acceleration phase, the velocity of the front drops until it gets to a state of constant velocity. In figure 2 we can clearly see the dependence of
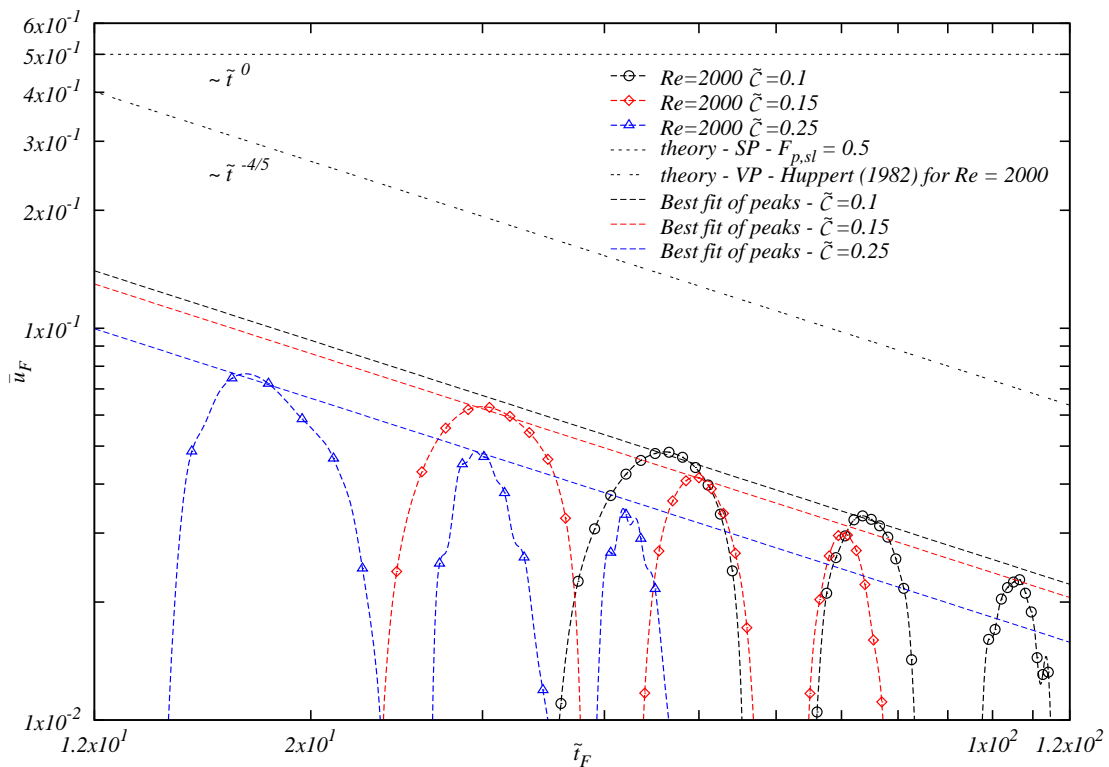
Figure 3: Front velocity $\overline{u}$ as a function of time $\tilde{t}$ during the viscous phase. The figure also include the scaling laws for the slumping and viscous phases with the best fit to the velocity peaks for the three cases with rotation.

this phase with the Coriolis parameter $\tilde{\mathcal{C}}$. As $\tilde{\mathcal{C}}$ increases, the constant slumping phase velocity drops. This variation is more noticeable in case 3 for $\tilde{\mathcal{C}} = 0.25$, and the period of constant velocity is very small. Based on this trend, we can expect to see a more rapid variation in the front velocity as we increase $\tilde{\mathcal{C}}$, with an eventual absence of the slumping phase.

For our simulations, we calculate the mean velocity for the period of constant velocity, and in case 3, for the period of slower variation in velocity. These values are 0.399, 0.388, 0.377 and 0.337 for $\tilde{\mathcal{C}} = 0$, 0.1, 0.15 and 0.25, respectively.

The dimensionless front velocities of our simulations are lower in comparison with the value predicted by the hydraulic theories for full depth release (1/2). This is in good agreement with simulations of planar currents presented by Cantero et al. (2007b), Necker et al. (2002), and laboratory experiments by Rottman and Simpson (1983) and Marino et al. (2005).

Although the mean velocity in the slumping phase drops with the increase of the Coriolis parameter, the near constant velocity is observed in the same interval of time $2.5 < \tilde{t} < 4.7$ for cases with rotation. As expected, the corresponding front location interval decreases with the increase of the Coriolis force produced by the rotation of the system. The front location intervals for constant velocity in the slumping phase are $0.9 < \overline{x}_F - \overline{x}_0 < 1.8$ for $\tilde{\mathcal{C}} = 0.1$, $0.9 < \overline{x}_F - \overline{x}_0 < 1.7$ for $\tilde{\mathcal{C}} = 0.15$, and $0.9 < \overline{x}_F - \overline{x}_0 < 1.6$ for $\tilde{\mathcal{C}} = 0.25$.

4.2.3 Inertial and viscous phases

After the interval of constant velocity at $\tilde{t} = 4.7$ where the fronts have traveled between 1.6 and 1.8 lock lengths, we observe in all cases with rotation (see Fig. 2) a rapid drop in front velocity, until it gets to a value of zero, from when the front starts to propagate inward (negative
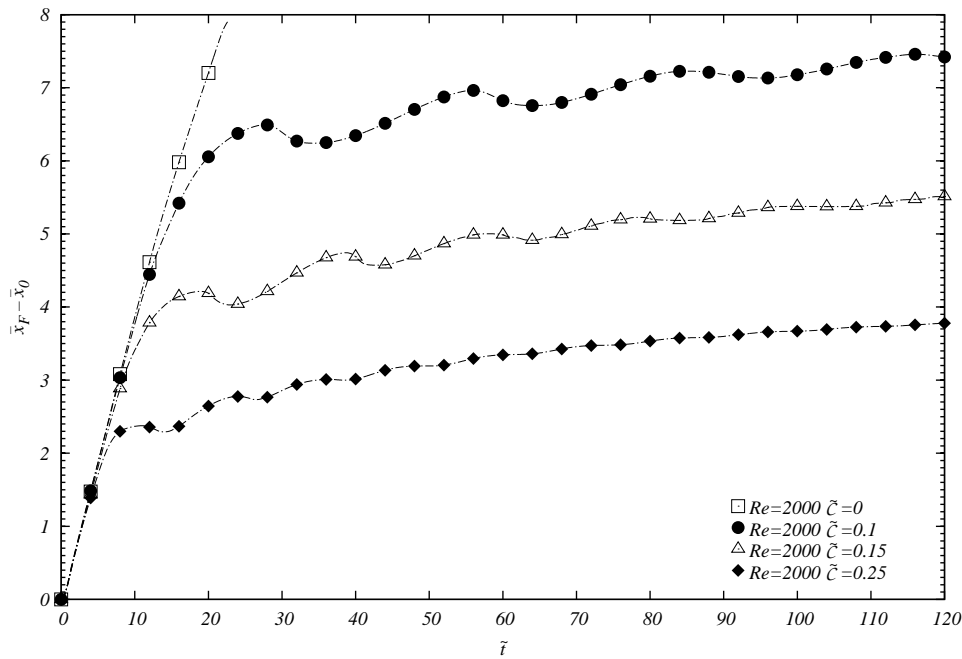
Figure 4: Location of the front relative to the initial position $\overline{x}_F - \overline{x}_0$ as a function of time $\tilde{t}$.

values of $\overline{u}_F$). This phenomenon will be studied in the next section.

We then observe successive pulses of the front location (see Fig. 4), with corresponding front velocity oscillations (see Fig. 3). The value of these peaks decreases, following a decaying law with a slope in good agreement with predictions made by Huppert (1982) for the viscous phase in planar currents, with $Re = 2000$ and $\xi_{pHp} = 3.2$ (see Eq. 13). Figure 3 shows an overestimation made by these predictions owing to the presence of rotation in our simulations. The best fit to the values of the peaks in velocity gives $\xi_{pHp} = 1.12$, 1.04 and 0.79 for $\tilde{\mathcal{C}} = 0.1$, 0.15 and 0.25, respectively (see Fig. 3).

In case 0 ($\tilde{\mathcal{C}} = 0$), the drop in velocity after the slumping phase is in good agreement with the predictions made by Huppert (1982) and Cantero et al. (2007b) (see Fig. 2). The absence of an inertial phase in all our simulations will be discussed in the next section.

4.3   Transition between phases

Following Cantero et al. (2007b), the transition points between phases of spreading can be computed by matching the front velocity of the corresponding scaling laws at the time of transition. The constants of the scaling laws we use are $\xi_p = 1.47$ and $\xi_{pHp} = 3.2$ (see equations (12) and (13)), determined by Cantero et al. (2007b) from experimental data.

First we match the constant velocity of the slumping phase $F_{p,sl}$ with the front velocity of the inertial phase (see Eq. 12). The time of transition from slumping to inertial phase is then given by

$$\tilde{t}_{SI} = \left(\frac{2}{3}\xi_p\right)^3 \frac{\overline{x}_0 \overline{h}_0}{F_{p,sl}^3} . \tag{17}$$

The values of $F_{p,sl}$ for $\tilde{\mathcal{C}} = 0$, 0.1, 0.15 and 0.25 are 0.399, 0.388, 0.377 and 0.337, respectively. For these values and with $\overline{x}_0 = \overline{h}_0 = 1$, the times of transition from slumping to inertial phase are $\tilde{t}_{SI} = 14.84$, 16.01, 17.41 and 24.32 for $\tilde{\mathcal{C}} = 0$, 0.1, 0.15 and 0.25, respectively. The

location of where this transition occur can be determined as

$$\frac{x_{SI}}{x_0} = \frac{u_F t_{SI}}{x_0} = \left(\frac{2\xi_p}{3}\right)^3 \left(\frac{F_{p,sl}}{\overline{h}_0^{1/2}}\right)^{-2} , \tag{18}$$

and using the values of $F_{p,sl}$ obtained for our simulations and $\xi_p = 1.47$, we get $\tilde{x}_{SI} = 5.918$, 6.25, 6.58 and 8.23 for $\tilde{\mathcal{C}} = 0$, 0.1, 0.15 and 0.25, respectively.

The second transition time of our interest is from the slumping phase directly to the viscous phase $\tilde{t}_{SV}$, obtained by matching the constant front velocity of the slumping phase and the velocity of the viscous phase (see Eq. 13). This gives

$$\tilde{t}_{SV} = \left(\frac{1}{5}\xi_{pHp}\right)^{5/4} \frac{\left(\overline{x}_0\overline{h}_0\right)^{3/4}}{F_{p,sl}^{5/4}} Re^{1/4} , \tag{19}$$

and with the values of $F_{p,sl}$ presented earlier and the constant $\xi_{pHp} = 3.2$ obtained by Cantero et al. (2007b), the times of transition between slumping to viscous phases for $\tilde{\mathcal{C}} = 0$, 0.1, 0.15 and 0.25 are $\tilde{t}_{SV} = 12.08$, 12.49, 12.91 and 14.84, respectively. Comparing these values with the values obtained for $\tilde{t}_{SI}$, we can see that $\tilde{t}_{SV}$ is smaller than $\tilde{t}_{SI}$ in all cases. This evidence the absence of the inertial phase seen in our simulations. For case 0 ($\tilde{\mathcal{C}} = 0$), $\tilde{t}_{SV} = 12.08$ is in good agreement with figure 3, where we can see the departure from constant velocity at about $\tilde{t} = 12$.

The slumping to inertial phase transition time (Eq. 17) has a weak Reynolds-number dependence through $F_{p,sl}$ and becomes independent only at large Re. In contrast, the transition time between slumping to viscous phases $\tilde{t}_{SV}$ will increase with Re. Thus, at lower Re, $\tilde{t}_{SV}$ become smaller than $\tilde{t}_{SI}$, and a direct transition between the slumping and the viscous phase occurs. Cantero et al. (2007b) studied in detail the transition time dependence with Re, and matching (17) with (19) estimated that the critical Re for the inertial phase to exist is $Re_{cr} = 2000\overline{x}_0\overline{h}_0$. This is in good agreement with our results.

For our simulations, the increasing difference between $\tilde{t}_{SI}$ and $\tilde{t}_{SV}$ as $\tilde{\mathcal{C}}$ increase, suggest a dependence between the existence of the inertial phase and the speed of rotation of the system.

4.4 Maximum distance of propagation

After the release of the dense fluid, the initial behavior of the rotating currents is similar to that of the non-rotating current. After a certain time, the deceleration of the rotating currents is evident until the velocity of the fronts $\overline{u}_F$ becomes zero. We define the location in the streamwise direction were velocity becomes zero as $\overline{x}_{max}$. The location of the front relative to the initial position $\overline{x}_F - \overline{x}_0$ as a function of time $\tilde{t}$ is displayed in Fig. 4.

The maximum distances of propagation of the fronts are shown from Fig. 5 for cases (1) to (3). As we can see, the maximum distance of propagation of the first outward pulse of dense fluid is influenced by the rotation of the system. With the increase of the Coriolis parameter, less propagation of the front occurs. Also, this steady-state happens before in case 3 (with larger Coriolis parameter) than in the other cases. The values of $\overline{x}_{max}$ are shown in Table 1.

Figure 6 shows the relation between the maximum distance of propagation of the first outward pulse of dense fluid ($\overline{x}_{max} - \overline{x}_0$) and the Coriolis parameter $\tilde{\mathcal{C}}$. The best fit to the data yields

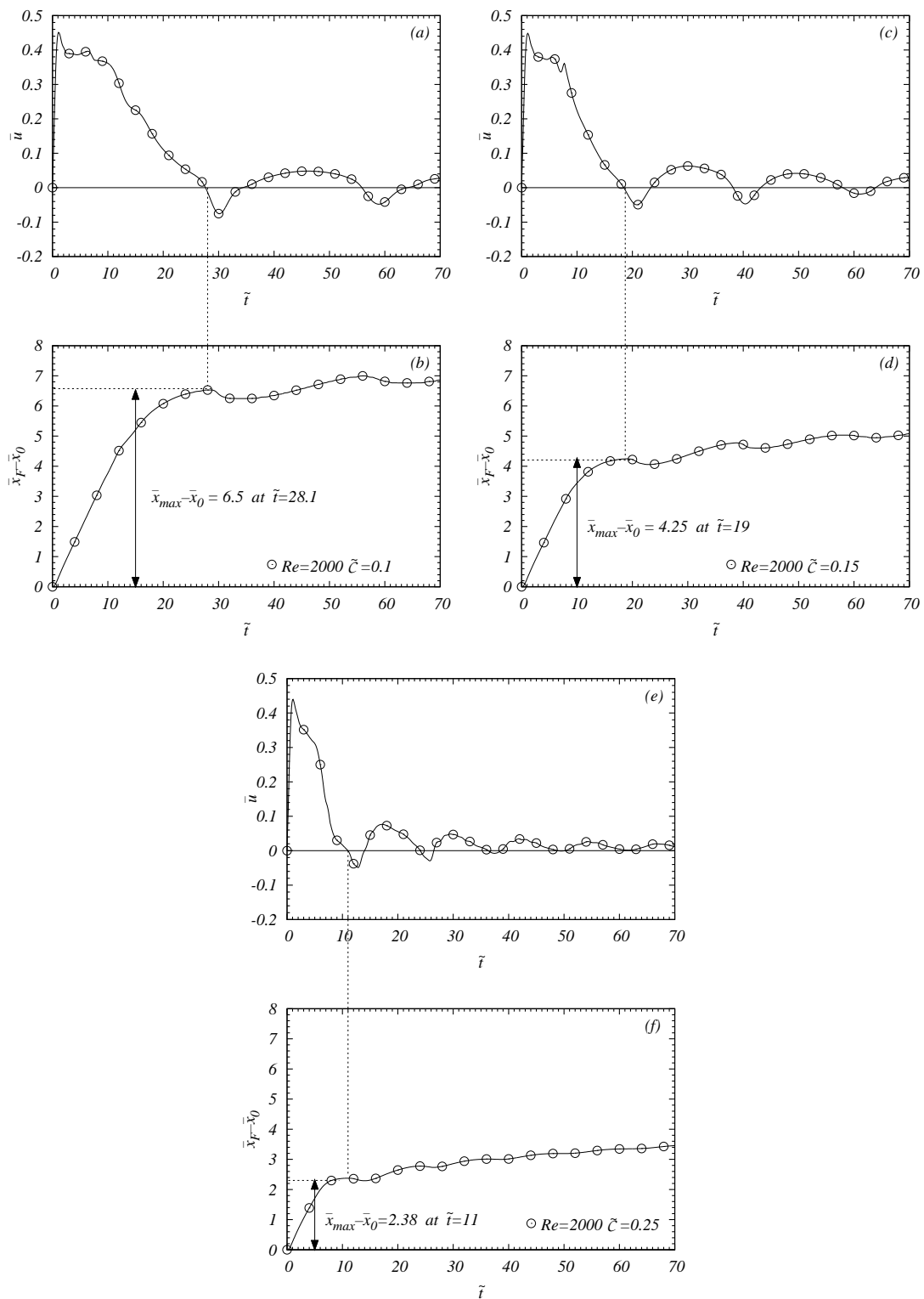$$\overline{x}_{max} = 1 + \frac{1}{1.56\tilde{\mathcal{C}}} , \tag{20}$$

Figure 5: Maximum distance of propagation relative to the initial position for cases 1 to 3. a) Velocity of the front $\overline{u}_F$ as a function of time $\tilde{t}$ for case 1; b) Location of the front relative to the initial position $\overline{x}_F - \overline{x}_0$ as a function of time $\tilde{t}$ for case 1; c) Velocity of the front $\overline{u}_F$ as a function of time $\tilde{t}$ for case 2; d) Location of the front relative to the initial position $\overline{x}_F - \overline{x}_0$ as a function of time $\tilde{t}$ for case 2; e) Velocity of the front $\overline{u}_F$ as a function of time $\tilde{t}$ for case 3; f) Location of the front relative to the initial position $\overline{x}_F - \overline{x}_0$ as a function of time $\tilde{t}$ for case 3.
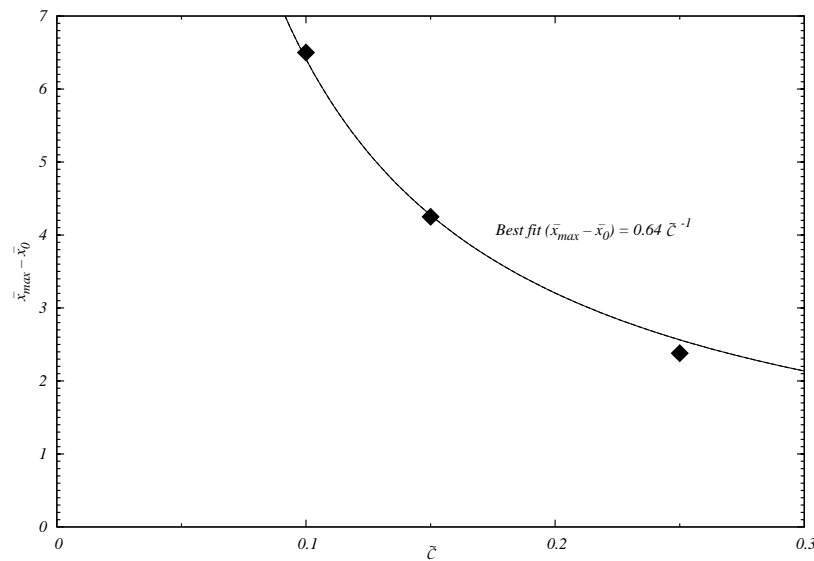
Figure 6: Maximum distance of propagation $\overline{x}_{max} - \overline{x}_0$ in the streamwise direction as a function of Coriolis parameter $\tilde{\mathcal{C}}$.

4.5 Frequency of the fronts

Prior to the arrest of the initial front, a reverse flow in the tail of the current, and a contraction and increase of thickness of the current towards $\overline{x} = 0$ is observed. This accumulation of fluid relaxes and produces a second outward propagating pulse of dense fluid that exceed $\overline{x}_{max}$ of the first propagating pulse of fluid. This behavior repeats itself several times.

Figure 7 shows the results for density function $\tilde{\rho}$ contours at $\tilde{y} = 0.5$ for case (2) at various time instances. At $\tilde{t} = 5$, the first outward pulse of fluid is visible. At time $\tilde{t} = 10$ and soon after at $\tilde{t} = 15$, the reverse flow advance towards $\overline{x} = 0$.

The mean pulse period $\overline{T}_p$ for each case, defined as the averaged time interval on which the successive outward pulses reach $\overline{u}_F = 0$. The pulse frequency $\overline{\omega}_p$ is defined as

$$\overline{\omega}_p = \frac{2\pi}{\overline{T}_p} \,. \tag{21}$$

The values of $\overline{\omega}_p$ are shown in Table 1. Figure 8 suggest a linear dependence of $\overline{\omega}_p$ with the Coriolis parameter $\tilde{\mathcal{C}}$

$$\overline{\omega}_p = K\tilde{\mathcal{C}} \,. \tag{22}$$

The best-fit yields $K = 2.02$. Similar results were found by Hallworth et al. (2001) with laboratory experiments of axisymmetric gravity currents. Figure 9 shows the mean pulse period and frequency for cases (1) to (3).
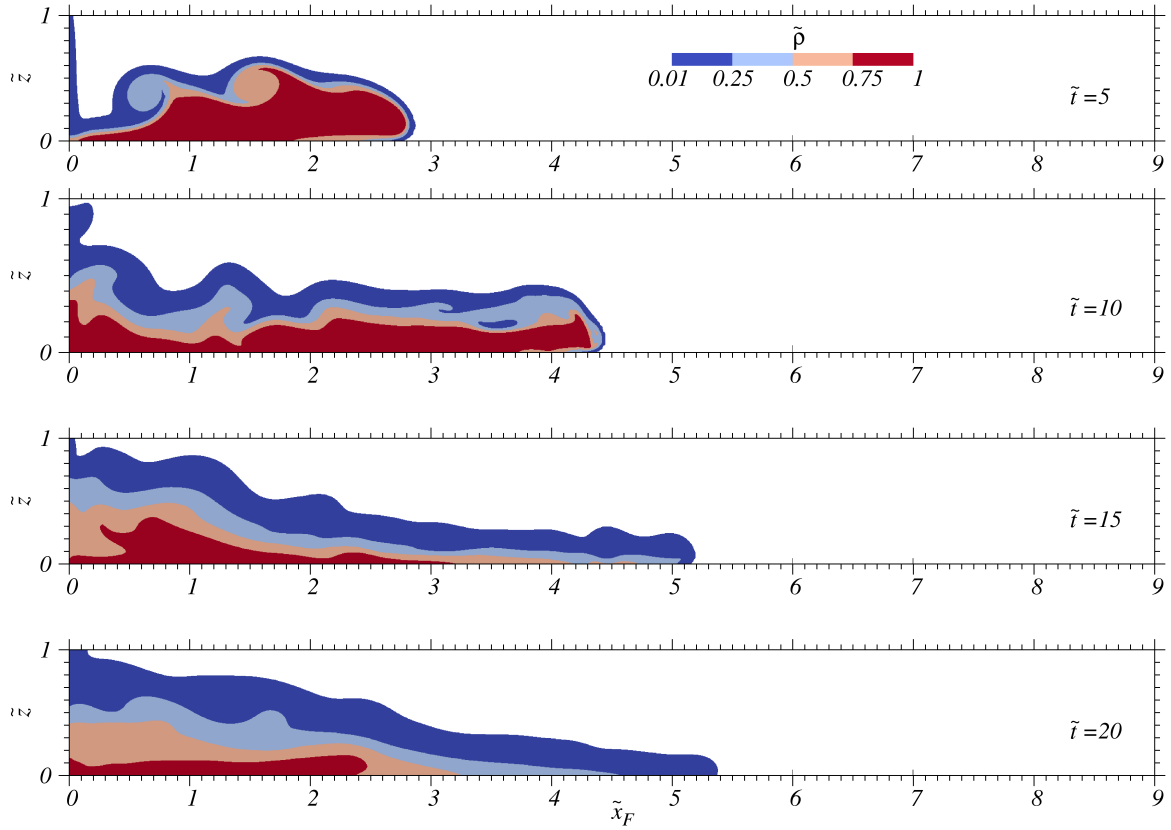
Figure 7: Results for the density function $\tilde{\rho}$ at $\tilde{y} = 0.5$ for case (2) at different times.
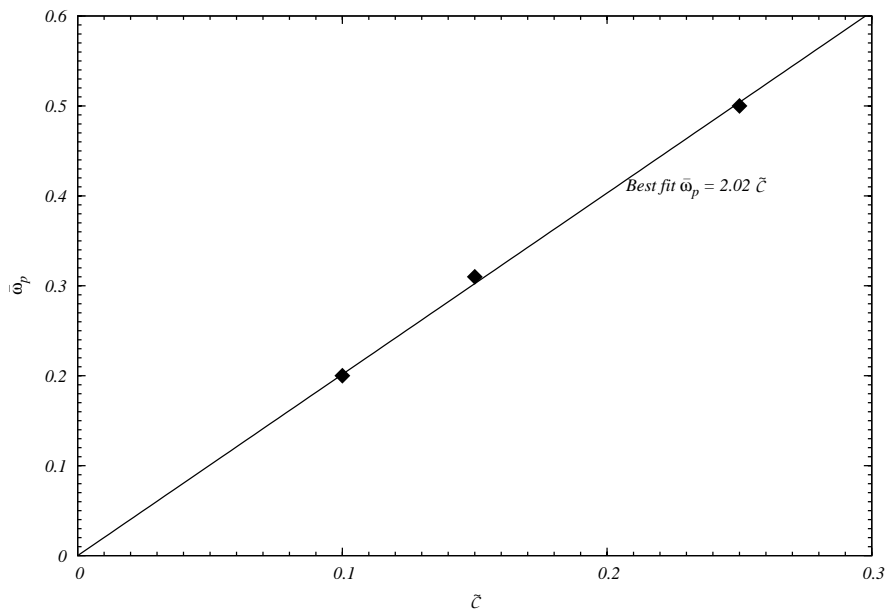

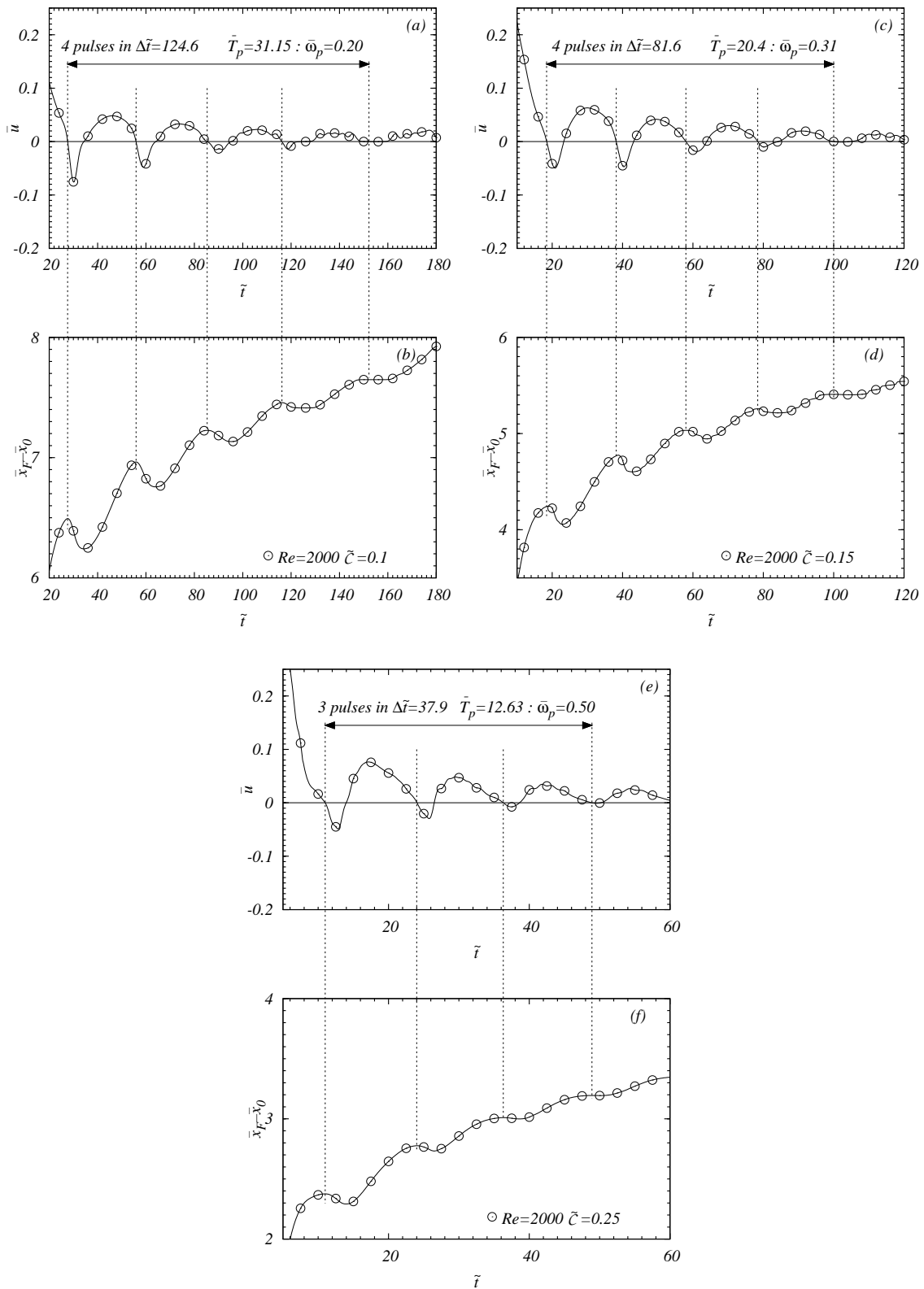Figure 8: Mean pulse frequency $\overline{\omega}_p$ as a function of the Coriolis parameter $\tilde{\mathcal{C}}$.

Figure 9: Mean pulse period $\overline{T}_p$ and the pulse frequency $\overline{\omega}_p$ for cases 1 to 3. a) Velocity of the front $\overline{u}_F$ as a function of time $\tilde{t}$ for case 1. b) Location of the front relative to the initial position $\overline{x}_F - \overline{x}_0$ as a function of time $\tilde{t}$ for case 1. c) Velocity of the front $\overline{u}_F$ as a function of time $\tilde{t}$ for case 2. d) Location of the front relative to the initial position $\overline{x}_F - \overline{x}_0$ as a function of time $\tilde{t}$ for case 2. e) Velocity of the front $\overline{u}_F$ as a function of time $\tilde{t}$ for case 3. f) Location of the front relative to the initial position $\overline{x}_F - \overline{x}_0$ as a function of time $\tilde{t}$ for case 3.

5   CONCLUSIONS

In the present work we studied stratified currents in a periodic channel with rotation effects by direct numerical simulation. The flow was initiated from a solid rotating state at a constant velocity Ω.

We compared cases with different Coriolis parameters $\tilde{\mathcal{C}}$ and found significant differences in the different phases of spreading. The maximum velocity in the acceleration phase drops when $\tilde{\mathcal{C}}$ is increased, however, the location and time where this peak happens is insensitive to $\tilde{\mathcal{C}}$. A similar relation was found between the constant velocity in the slumping phase and the Coriolis parameter, where the velocity drops as $\tilde{\mathcal{C}}$ increases, but the time interval when it happens is the same for cases with $\tilde{\mathcal{C}} > 0$. Based on the trend of the constant velocity, a more rapid variation is expected as we increase the Coriolis parameter with the eventual absence of the slumping phase.

After the phase of constant velocity, the rotation of the system produces a rapid drop in front velocity, until it gets to a value of zero, from when the front starts to propagate inward and outward repeatedly. The values of peak velocity follow a decaying law with a slope in good agreement with predictions made by Huppert (1982) for the viscous phase, but overestimated by this predictions owing to rotation.

The absence of an inertial phase is evidenced by the relation of the times of transition between each phase. For all our simulations, the transition time between the slumping to viscous phase ($\tilde{t}_{SV}$) is smaller than that of the slumping to inertial phase ($\tilde{t}_{SI}$), and the increase of the difference suggests a dependence of the existence of the inertial phase with the Coriolis parameter.

The maximum distance of propagation of the first pulse in the front, where the velocity of the front becomes zero, is restricted by rotation, and as we increase $\tilde{\mathcal{C}}$, less propagation in the streamwise direction occurs.

Before the arrest of the first propagating front, a reverse flow in the tail of the current is observed, generating an accumulation of fluid towards the initial position of the dense fluid that relaxes and produces a second outward front. The mean pulse frequency appears to be linearly dependent of the Coriolis factor with a relation $\overline{\omega_p} = 2.02\tilde{\mathcal{C}}$.

REFERENCES

Benjamin T. Gravity currents and related phenomena. *Journal of Fluid Mechanics*, 31:209–248, 1968.

Cantero M., Balachandar S., and García M. Highly resolved simulations of cylindrical density currents. *Journal of Fluid Mechanics*, 590:437–469, 2007a.

Cantero M., Balachandar S., García M., and Ferry J. Direct numerical simulations of planar and cyindrical density currents. *Journal of Applied Mechanics*, 73:923–930, 2006.

Cantero M., Lee J.R., Balachandar S., and García M. On the front velocity of gravity currents. *Journal of Fluid Mechanics*, 586:1–39, 2007b.

Canuto C., Hussaini M., Quarteroni A., and Zang T. *Spectral Methods in Fluid Dynamics*. Springer-Verlag, New York, 1988. 557 pages.

Choi S.U. and García M. k-ε turbulence modeling of density currents developing two dimensionally on a slope. *Journal of Hydraulic Engineering*, 128(1):55–63, 2002.

Droegemeier K. and Wilhelmson R. Kelvin-Helmholtz instability in a numerically simulated thunderstorm outflow. *Bulletin of the American Meteorological Society*, 67(4):416–417, 1986.

Droegemeier K. and Wilhelmson R. Numerical simulation of thunderstorm outflows dynamics. Part I: Outflow sensitivity experiments and turbulence dynamics. *Journal of the Atmospheric Sciences*, 44(8):1180–1210, 1987.

Durran D. *Numerical Methods for Wave Equations in Geophysical Fluid Dynamics*. Springer, 1999.

Fannelop T. and Waldman G. The dynamics of oil slicks – or 'creeping crude. *A.I.A.A. J.*, 41:1–10, 1971.

Fay J. The spreads of oil slicks on a calm sea. In D.P. Hoult, editor, *Oils in the sea*, pages 53–63. Plenum, 1969.

García M. Turbidity currents. In L. Brekhovskikh, K. Turekian, K. Emery, and C. Tseng, editors, *Encyclopedia of Earth System Science*, volume 4, pages 399–408. Academic Press, Inc., New York, 1992.

Hallworth M., Huppert H., and Ungarish M. Axisymmetric gravity currents in a rotating system: experimental and numerical investigations. *Journal of Fluid Mechanics*, 447:1–29, 2001.

Hoult D. Oil spreading in the sea. *Ann. Rev. Fluid Mechanics*, 4:341–368, 1972.

Huppert H. The propagation of two-dimensional and axisymmetric viscous gravity currents over a rigid horizontal surface. *Journal of Fliud Mechanics*, 121:43–58, 1982.

Huppert H. and Simpson J. The slumping of gravity currents. *Journal of Fluid Mechanics*, 99:785–799, 1980.

Marino B., Thomas L., and Linden P. The front condition for gravity currents. *Journal of Fluid Mechanics*, 536:49–78, 2005.

Metha A., Sutherland B., and Kyba P. Interfacial gravity currents. II. Wave excitation. *Physics of Fluids*, 14(10):3558–3569, 2002.

Necker F., Härtel C., Kleiser L., and Meiburg E. High-resolution simulations of particle-driven gravity currents. *International Journal of Multiphase Flow*, 28:279–300, 2002.

Rottman J. and Simpson J. Gravity currents produced by instantaneous releases of a heavy fluid in a rectangular channel. *Journal of Fluid Mechanics*, 135:95–110, 1983.

Shin J., Dalziel S., and Linden P. Gravity currents produced by lock exchange. *Journal of Fluid Mechanics*, 521:1–34, 2004.

Ungarish M.M. *An introduction to gravity currents and intrusions*. CRC Press, 2009.